

Regimes in astrophysical lensing: refractive optics, diffractive optics, and the Fresnel scale

Dylan L. Jow,^{2,3}★ Ue-Li Pen,^{1,2,3,4,5,6} and Job Feldbrugge^{7,8}

¹*Institute of Astronomy and Astrophysics, Academia Sinica, Astronomy-Mathematics Building, No. 1, Section 4, Roosevelt Road, Taipei 10617, Taiwan*

²*Canadian Institute for Theoretical Astrophysics, University of Toronto, 60 St. George Street, Toronto, ON M5S 3H8, Canada*

³*Department of Physics, University of Toronto, 60 St. George Street, Toronto, ON M5S 1A7, Canada*

⁴*Perimeter Institute for Theoretical Physics, 31 Caroline St. North, Waterloo, ON, Canada N2L 2Y5*

⁵*Canadian Institute for Advanced Research, CIFAR program in Gravitation and Cosmology*

⁶*Dunlap Institute for Astronomy & Astrophysics, University of Toronto, AB 120-50 St. George Street, Toronto, ON M5S 3H4, Canada*

⁷*Higgs Centre for Theoretical Physics, James Clerk Maxwell Building, Edinburgh EH9 3FD, UK*

⁸*Department of Physics, Carnegie Mellon University, 5000 Forbes Ave, Pittsburgh, PA 15217, USA*

Accepted XXX. Received YYY; in original form ZZZ

ABSTRACT

Astrophysical lensing has typically been studied in two regimes: diffractive optics and refractive optics. Diffractive optics is characterized by a perturbative expansion of the Kirchhoff-Fresnel diffraction integral, while refractive optics is characterized by the stationary phase approximation. Previously, it has been assumed that the Fresnel scale, R_F , is the relevant physical scale that separates these two regimes. With the recent introduction of Picard-Lefschetz theory to the field of lensing, it has become possible to generalize the refractive description of discrete images to all wave parameters, and, in particular, exactly evaluate the diffraction integral at all frequencies. In this work, we assess the regimes of validity of refractive and diffractive approximations for a simple one-dimensional lens model through comparison with this exact evaluation. We find that, contrary to previous assumptions, the true separation scale between these regimes is given by $R_F/\sqrt{\kappa}$, where κ is the convergence of the lens. Thus, when the lens is strong, refractive optics can hold for arbitrarily small scales. We also argue that intensity variations in diffractive optics are generically small, which has implications for the study of strong diffractive scintillation (DISS).

Key words: waves – radio continuum: ISM – pulsars:general – fast radio bursts

1 INTRODUCTION

When coherent sources, such as pulsars and fast radio bursts (FRBs), undergo lensing, wave effects become important. Pulsar scintillation, for example, is due to the interference of many coherent images formed due to scattering in the interstellar medium (ISM). As more data of these coherent sources becomes available from current and future observations, there has been increased interest in the study of wave optics in the context of astrophysical lensing (see e.g. Grillo & Cordes 2018; Main et al. 2018; Feldbrugge et al. 2019; Feldbrugge & Turok 2020; Feldbrugge 2020; Jow et al. 2020; Shi & Xu 2021).

In principle, wave optics is fully described by the Kirchhoff-Fresnel diffraction integral, which is a path integral over all paths connecting the source and observer through a refractive medium. In practice, however, the full diffraction integral is rarely computed, as there exist few analytic solutions for lenses of interest, and its highly oscillatory nature makes it challenging to compute numeri-

cally. It has only been through the recent application of the mathematical framework of Picard-Lefschetz theory that computing the diffraction integral exactly has become numerically tractable (see e.g. Feldbrugge et al. 2019; Feldbrugge & Turok 2020; Feldbrugge 2020; Jow et al. 2021; Shi & Xu 2021). Previously, astrophysical lensing has typically been studied in the geometric regime, where the contribution to the observed flux is isolated to a discrete set of well-defined images whose individual fluxes can be easily computed. Wave effects are then added, to first order, by computing the phase associated with each image and allowing them to coherently interfere at the observer. This is also known as the Eikonal limit, which is equivalent to the stationary-phase approximation of the diffraction integral¹.

¹ Note that some authors make a distinction between geometric optics and the Eikonal limit of wave optics, where geometric optics is when the images are added incoherently at the observer and the Eikonal limit is when they are added coherently. Here we will use the terms “geometric optics” and “Eikonal limit” interchangeably to refer to the regime where isolated images interfere coherently.

★ E-mail: djow@physics.utoronto.ca

Geometric optics, or the Eikonal limit, is the high-frequency limit of the Kirchhoff-Fresnel integral. The low-frequency limit of optics has also been studied, as it is often possible to compute the Kirchhoff-Fresnel integral through a perturbative expansion. In the plasma lensing literature, these two limits of optics (geometric and perturbative) are sometimes referred to as the refractive and diffractive regimes, respectively, as the geometric limit is characterized by a discrete set of isolated images that are refracted into the direction of the observer, whereas the perturbative regime is characterized by contributions to the diffraction integral from an extended area on the sky (see e.g. [Rickett 1990](#); [Lorimer & Kramer 2012](#)).

It is of central importance to the study of wave optics to understand at what frequency these two regimes become valid, and whether or not there is any overlap. In the absence of an exact result for the Kirchhoff-Fresnel integral, it has often been assumed in the literature that the Fresnel scale sets the frequency which separates geometric optics from the diffractive regime (see e.g. [Cordes et al. 1986](#); [Lorimer & Kramer 2012](#); [Pen & King 2012](#); [Johnson et al. 2018](#); [Er et al. 2022](#)). In this work, however, we will show that the Fresnel scale is, generically, the wrong scale. Rather, a combination of the Fresnel scale and lens strength sets the correct separation scale between the geometric and diffractive regimes.

It is by employing the mathematical framework of Picard-Lefschetz theory that we are able to make a detailed study of the transition from refractive optics to diffractive optics. Not only does Picard-Lefschetz theory allow for an exact evaluation of the Kirchhoff-Fresnel integral at all frequencies that we can quantitatively compare to the various approximations, it also allows for a well-defined separation of the integral into contributions from a discrete set of images at all frequencies, which, in the high-frequency limit, agrees with the geometric images. As such, Picard-Lefschetz theory bridges the conceptual gap between the image description of geometric optics and the perturbative description of the diffractive regime.

This paper is structured in the following way. In Section 2, we will review the stationary-phase approximation which is used to compute geometric optics, as well as the perturbative expansion which can be used to approximate the diffraction integral in the low-frequency limit. In Section 3, we will study a simple 1D rational lens to argue that most of parameter space is well described by either of these two approximations, and that the separation scale between the two regimes is given by the Fresnel scale divided by the square-root of the convergence. Contrary to what has previously been assumed in much of the lensing literature, the separation scale is *not* the Fresnel scale alone. Indeed, for either large or small lens strengths, the Fresnel scale may be off by orders-of-magnitude. In Section 4, we will argue that lensing in the diffractive regime is typically weak, and therefore an observation of strong scintillation already suggests lensing in the refractive regime. In Section 5 we show how the two regimes behave differently in delay space. Our numerical results are quite general and can be applied to scenarios in gravitational lensing and plasma lensing, as well as potential applications to scattering theory in quantum mechanics. However, in Section 6, we discuss in greater detail the connection between our results and previous results in the literature on turbulent plasma lensing. In Appendix A, we present the detailed Picard-Lefschetz analysis of the rational lens.

We note that while our focus will be astrophysical lensing, our results may be applicable to problems in scattering theory in quantum mechanics. In particular, while we focus on single-plane lensing, the formalism for multi-plane lensing is equivalent to the real-time Feynman path integral in the limit of infinite planes using

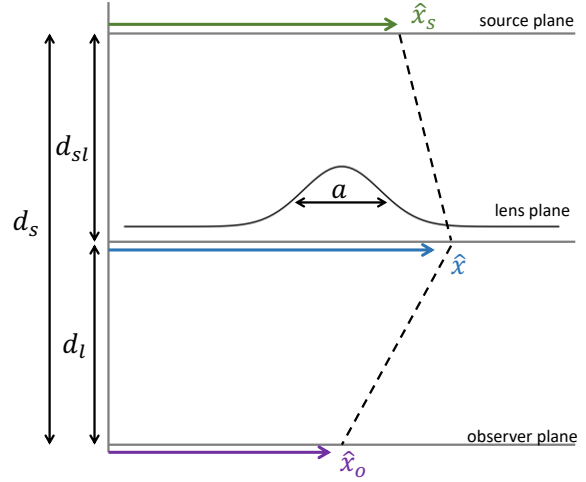


Figure 1. Diagram of thin-plasma lensing showing distances and coordinates involved.

the time-slicing approximation. In this setting, the diffractive limit corresponds to the application of perturbative methods resulting in the Feynman rules, whereas the refractive limit corresponds to non-perturbative methods such as the use of instantons and the study of (complex) classical trajectories. The tools of Picard-Lefschetz theory, which we use here to evaluate the Kirchhoff-Fresnel integral, have been recently used to evaluate the Feynman path integral to reinterpret phenomena in quantum mechanics ([Turok 2014](#); [Cherman & Unsal 2014](#); [Tanizaki & Koike 2014](#); [Gozzi et al. 2021](#)).

2 THE PERTURBATIVE EXPANSION AND EIKONAL APPROXIMATION OF WAVE OPTICS

The flux at y of a source lensed by a thin screen can be expressed as the magnitude $|F(y)|^2$, where the amplitude F is obtained from the dimensionless Kirchhoff-Fresnel diffraction integral

$$F(y) = \sqrt{\frac{\nu}{2\pi i}} \int_{-\infty}^{\infty} e^{i\nu \left[\frac{(x-y)^2}{2} + \kappa\psi(x) \right]} dx, \quad (1)$$

with the phase variation induced by the lens given by ψ and where we integrate over all possible paths from the source to the observer intersecting the lens plane at x . For convenience, we use the dimensionless version of the Kirchhoff-Fresnel integral with the dimensionless relative position of source and observer, frequency, and lens strength y , ν , and κ . Fig. 1 shows a diagram of the lensing setup, with dimensionful parameters. The dimensionless parameters in Eq. (1) are related to these by $x = \hat{x}/a$, where a is some length scale associated with the lens, $y = \hat{y}/a = (\hat{x}_s d_l + \hat{x}_o d_{sl})/ad_s$, and $\nu = \omega a^2/c\bar{d}$ where $\bar{d} = d_{sl}d_l/d_s$. In the following sections, we will refer only to the dimensionless parameters so that our analysis can be easily applied to a wide variety of contexts. We will further discuss the underlying physical parameters in the context of plasma and gravitational lensing in Sections 6 and 7. See also [Schneider et al. \(1992\)](#), [Nakamura & Deguchi \(1999\)](#), [Feldbrugge et al. \(2019\)](#) and [Jow et al. \(2021\)](#) for a more thorough discussion of the correspondence of these dimensionless parameters to physical parameters in different contexts.

In this work, we restrict our attention to the case of a one-dimensional lens, with a single peak, and we make a choice of

co-ordinates x and y such that the peak is centred at $x = 0$ and has curvature $\psi''(0) = -2$. Under this choice of coordinates, the parameter κ is the convergence of the lens (Pen & King 2012; Schneider et al. 1992). A canonical example of such a lens is the Gaussian lens, $\psi(x) = \exp\{-x^2\}$, which has been used in many lensing studies (see, e.g., Clegg et al. 1998; Pen & King 2012; Cordes et al. 2017). One may also construct rational approximations of the Gaussian lens, such as the simple rational lens, $\psi(x) = 1/(1+x^2)$, which corresponds to the first-order Padé approximation of the Gaussian potential. For the sake of simplicity, we will also restrict our attention to convergent lenses, i.e. $\kappa > 0$.

The Kirchhoff-Fresnel integral is equivalent to a path integral through the lens plane with phase $S(x, y; \nu, \kappa) = \nu[\frac{(x-y)^2}{2} + \kappa\psi(x)]$. Geometric optics is obtained in the high-frequency limit ($\nu \rightarrow \infty$), through the stationary-phase approximation. That is, in geometric optics, the contributions to the Kirchhoff-Fresnel integral reduce to a discrete set of isolated points, or images, $\{x_j\}$, which have stationary phase, $\partial_x S(x_j) = 0$. The condition of stationary phase gives rise to the lens map,

$$\xi(x) \equiv y = x + \kappa\psi'(x), \quad (2)$$

which maps points on the lens plane to a source position y . For a given source position, the images, $\{x_j\}$, with stationary phase, are solutions to the lens equation, $\xi(x) = y$. Note that while the map ξ is one-to-one, the inverse map ξ^{-1} need not be, and a given source position may correspond to multiple images.

In the geometric, or stationary-phase approximation, each individual image has an associated wave-field given by

$$F_j^{\text{geom.}} = \frac{1}{|\Delta_j|^{1/2}} e^{iS(x_j, y; \nu, \kappa) - i\frac{\pi}{2}n_j}, \quad (3)$$

where $\Delta_j = \xi'(x_j)$ is the Jacobian of the lens map, and n_j is the Morse index, which is 0 or 1 when x_j is a maximum or minimum of the lens map, respectively. The total wave-field at the observer in this limit is given by $F^{\text{geom.}} = \sum_j F_j^{\text{geom.}}$ (Schneider et al. 1992). This is also sometimes referred to as the Eikonal limit of wave optics. This approximation is valid in the limit $\nu \rightarrow \infty$, except at caustics, which are points where the lens map is degenerate, and $\Delta_j = 0$. At caustics, the intensity of the degenerate images formally goes to infinity. Despite this divergence, geometric optics is an extremely useful approximation in the high-frequency limit as the regions around the caustics at which the divergence occurs typically contribute very little overall flux.

So far we have assumed the lens map is a real map. However, generically the lens potential, ψ , and the associated lens map may be analytically continued so that the lens map can admit complex solutions (i.e. the images, x_j , may be complex). For such images, the wave-field is given by (Grillo & Cordes 2018)

$$F_j^{\text{geom.}} = \frac{1}{|\Delta_j|^{1/2}} e^{i[S(x_j, y; \nu, \kappa) - \frac{\arg(\Delta_j)}{2}]}. \quad (4)$$

Such an analytic continuation of the lens map actually improves the geometric approximation, and, indeed, is necessary to capture the behaviour of lensing just outside of caustics (Wright 1980; Grillo & Cordes 2018; Jow et al. 2020). Note, however, that not all complex solutions to the lens equation will contribute to the total flux. In general, determining whether or not a complex saddle point is relevant, i.e. whether or not it contributes to the total integral, requires computing the contour of steepest ascent in the function $h(x) = \text{Re}\{iS(x, y; \nu, \kappa)\}$ in the complex plane, originating at the saddle point. As we discuss in Appendix A, according to Picard-Lefschetz theory, whether or not the saddle point is relevant depends

on whether its steepest ascent contour intersects the real axis. The saddle point is relevant if and only if such an intersection exists. See, e.g., Jow et al. (2021) for a more detailed discussion of imaginary images in lensing. Note that real images are always relevant, because the steepest ascent contour originating from a real saddle point always intersects the real axis at the saddle point.

Now, the geometric or Eikonal limit is the high-frequency limit of the Kirchhoff-Fresnel integral. In order to apply this limit, it is necessary to know at what frequency it becomes a good approximation of the diffraction integral. It has sometimes been assumed that this frequency is set by the Fresnel scale (see e.g. Pen & King 2012; Er et al. 2022),

$$y_{\text{Frl}} \equiv 1/\sqrt{\nu}. \quad (5)$$

That is, if $y_{\text{Frl}} \ll 1$, then one is assumed to be firmly in the geometric regime. Note that y_{Frl} is the dimensionless version of the Fresnel scale given our parametrization of the Kirchhoff-Fresnel integral. Typically, the Fresnel scale is given as a distance scale, $R_F = \sqrt{\lambda d}/2\pi$, where λ is the wavelength of the light. In these units, the relevant limit is when the Fresnel scale is much smaller than the angular scale of the lens. One of the purposes of this work is to argue that the assumption that the Fresnel scale sets the frequency above which geometric optics holds is generically false.

Another tool for approximating the Kirchhoff-Fresnel diffraction integral is the perturbative expansion. In this approximation, one expands $\exp\{i\nu\kappa\psi(x)\} = 1 + i\nu\kappa\psi(x) + \dots$ in the integrand of the diffraction integral, giving

$$F^{\text{pert.}}(y) = 1 + i\nu\kappa\sqrt{\frac{\nu}{2\pi i}} \int e^{i\nu\frac{(x-y)^2}{2}} \psi(x) dx + \mathcal{O}((\kappa\nu)^2). \quad (6)$$

The small parameter that is being expanded in is given by

$$\epsilon \equiv \kappa\nu, \quad (7)$$

which we define here as it will later become of central importance.

The utility of performing this expansion is that for certain potentials, the first term is easier to compute analytically or numerically. For example, for the Gaussian lens, $\psi(x) = \exp\{-x^2/2\}$, the perturbative expansion can be computed to first order analytically as

$$F^{\text{pert.}}(y) = 1 + i\epsilon\sqrt{\frac{\nu}{2i + \nu}} e^{-\frac{\nu y^2}{2i + \nu}}. \quad (8)$$

Similarly, for the rational lens, $\psi(x) = 1/(1+x^2)$, one can compute the first-order expansion analytically as

$$\begin{aligned} F^{\text{pert.}}(y) &= 1 + i\frac{\epsilon}{2}\sqrt{\frac{-i\nu\pi}{2}} \left[e^{i\frac{\nu}{2}(y+i)^2} (1 + \text{erf}\{\sqrt{\frac{i\nu}{2}}(y+i)\}) \right. \\ &\quad \left. + e^{i\frac{\nu}{2}(y-i)^2} (1 + \text{erfc}\{\sqrt{\frac{-i\nu}{2}}(1+iy)\}) \right], \\ &\approx 1 + i\epsilon\sqrt{\frac{-i\nu\pi}{2}} e^{-\nu|y|} e^{i\frac{\nu}{2}(y^2-1)}, \end{aligned} \quad (9)$$

where the last approximation is valid for large $\nu|y|$. The first-order integral can be computed by first taking the integral in Fourier space by taking the Fourier transform of the potential, $\tilde{\psi}(k) = e^{-|k|}$.

When the perturbative expansion is valid, the flux at the observer can be described as a small oscillatory modulation about an un-lensed image. That is, when $\kappa = 0$ (i.e. when there is no lens), $F(y) \equiv F_0(y) = 1$, exactly. Thus, in the perturbative limit, the flux is described by a small modulation about the un-lensed flux, $F^{\text{pert.}}(y) = F_0(y) + i\epsilon g(y)$, for some function $g(y)$. This is what is sometimes referred to as the diffractive regime (Rickett 1990),

and it is qualitatively very distinct from geometric optics (a.k.a. the refractive regime). Whereas in geometric optics multiple isolated images form and interfere at the observer, the diffractive regime is effectively described by a single background image plus a small modulation.

Fig. 2 shows a schematic of the kind of lensing we are considering. A source emits radiation at some distance far from the lens and observer. The waves from the source encounter some lensing potential, $\psi(x)$, localized to the lens plane. This induces a phase variation in the wave front, which then propagates un-interrupted towards the observer, forming an interference pattern in the observer plane. The bottom panel shows the observed intensity computed for the rational lens for a fixed $\kappa = 5$ and different values of ν . For $\nu = 0.01$, the lensing is firmly in the diffractive limit and the intensity is well-described by a small oscillatory modulation about unity (note that in Fig. 2 the intensity fluctuations for $\nu = 0.01$ are multiplied by a factor of ten so that all three curves can be plotted on the same axis). For $\nu = 2$, the lensing is firmly in the refractive regime and is described by an interference pattern of multiple images. The curve for $\nu = 0.1$ is in a regime where neither the perturbative/diffractive or Eikonal/geometric approximations are good approximations.

The middle panel of Fig. 2 shows the light rays that pass through a given observer position, y . These rays correspond to the geometric images that an observer at y observes. Multiple rays may pass through an observer, and regions in the observer plane with different numbers of images per source position are separated by caustics (the caustics are easily visualized in the middle panel of Fig. 2). Now the field at the observer plane can be computed by assuming that each ray corresponds to a point source at the lens plane emitting a spherical wave with a relative phase determined by the lens. The field at the observer is then a sum of all of these spherical waves (this is known as the Huygens-Fresnel principle). Geometric optics arises when the frequencies are large, and so all the waves associated with rays that do not pass through the observer position y cancel out. Thus, the observed intensity in geometric optics is completely determined by the rays passing through a neighbourhood of the observer. In particular, the intensity of the individual images is given by the density of the rays passing through a small neighbourhood of the observer. Thus, in the geometric regime, the intensity curve traces the density of the rays passing through the observer plane. As ν decreases, the cross section of rays that contribute to the observed intensity at a given source position y becomes finite. As such, the interference between multiple images that is easily visible in the geometric regime gets washed out.

Note, that the perturbative expansion that gives rise to diffractive optics explicitly converges when the quantity $\epsilon \ll 1$. This is our first hint that the Fresnel scale may not be the relevant quantity for assessing when geometric optics holds. Given how qualitatively distinct the perturbative (diffractive) and geometric (refractive) descriptions are, the expectation is that there would not be a large region of parameter space where the two regimes overlap. However, if, indeed, geometric optics is valid whenever $y_{\text{Frl}} = 1/\sqrt{\nu} \ll 1$ (or, equivalently, when $\sqrt{\nu} \gg 1$), and the diffractive regime occurs whenever $\epsilon = \kappa\nu \ll 1$, then these two regimes should overlap for any given ν greater than unity, so long as κ is chosen to be sufficiently small. Another consequence of this would be that there would be large regions of parameter space that could neither be described by geometric optics, nor by the perturbative/diffractive expansion. As such, some alternative description of optics in this regime would be called for.

We argue that this is not, in fact, the case. Rather, contrary to previous assumptions, the Fresnel scale alone is not the appropriate

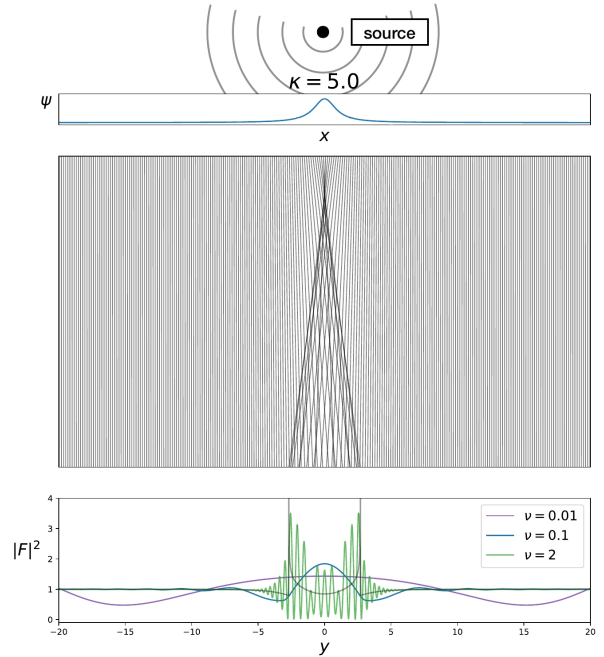


Figure 2. Schematic of thin-plane lensing. The source emits waves that scatter off of the lens potential, $\psi(x)$, localized to a lens plane (top panel). The lens induces a phase shift in the wave-front, which then propagates to the observer. The middle panel shows the light rays propagating from lens to observer, which correspond to the paths of stationary phase connecting source to observer, and are always perpendicular to the wave-front. The observed intensity as a function of observer position is shown in the bottom panel for fixed $\kappa = 5$ and different values of ν for the lens potential $\psi(x) = 1/(1+x^2)$. Note that the intensity fluctuations for $\nu = 0.01$ are multiplied by a factor of ten so that all three curves can be visualized on the same axis. The grey curve corresponds to the incoherent sum ($\sum_j |F_j|^2$) of the intensities of the images in the geometric limit.

quantity for determining when geometric optics is valid. Instead, a combination of the Fresnel scale and the convergence, $\epsilon = \kappa\nu$, sets both the scale below which the perturbative expansion is valid ($\epsilon \ll 1$), as well as the scale above which geometric optics holds ($\epsilon \gg 1$). In the next section, we will study a specific lens model to make this argument more concrete. In particular, by using Picard-Lefschetz theory to exactly evaluate the Kirchhoff-Fresnel integral at all frequencies, we can quantitatively determine when each of the two approximations we have described are valid.

3 A SIMPLE RATIONAL LENS

We will study the simple rational lens with potential given by

$$\psi(x) = \frac{1}{1+x^2}. \quad (11)$$

The lens map is given by

$$\xi(x) \equiv y = x - \frac{2\kappa x}{(1+x^2)^2}, \quad (12)$$

and its Jacobian takes the form

$$\xi'(x) = 1 + \frac{2\kappa(3x^2 - 1)}{(1+x^2)^3}. \quad (13)$$

The images corresponding to a position of the observer y – defined by the identity $\xi(x) = y$ – are roots of the fifth-order polynomial

$$x^5 - yx^4 + 2x^3 - 2yx^2 + (1 - 2\kappa)x - y = 0. \quad (14)$$

The quintic polynomial has five roots, either one or three of which being real depending on the position y . The real images are always relevant to the integral. The complex images emerge as conjugate pairs (since the polynomial is real), of which one is potentially relevant. By evaluating the intersections of the steepest ascent contour of the complex images and the real line, we determine the relevance of each complex saddle point (see Appendix A for a detailed discussion).

The perturbative/diffractive approximation of the lens integral is given by Eq. (9). We have chosen to study the rational lens as it has an analytic potential with a similar form to the more widely studied Gaussian lens; indeed, the potential is the first-order Padé approximation of the Gaussian potential $\psi(x) = \exp(-x^2/2)$. Thus, we expect the rational lens to behave similarly to the Gaussian lens. However, since the lens equation reduces to a simple fifth-order polynomial, there is only a small number of potentially relevant images, in contrast with the Gaussian lens, for which a potentially infinite number of images may be relevant, making the evaluation of the Kirchhoff-Fresnel integral much simpler for the rational lens. Once we have found the relevant images for the rational lens, we can evaluate the geometric or Eikonal approximation of the Kirchhoff-Fresnel integral. Our goal is to compare the regimes of validity of the geometric approximation and the perturbative/diffractive approximation given by Eq. (9).

In order to make this comparison, we use Picard-Lefschetz theory to numerically evaluate the Kirchhoff-Fresnel integral. As we discuss in Appendix A, Picard-Lefschetz theory allows for an exact evaluation of the diffraction integral at arbitrary frequencies. Thus, we are able to compare the various approximations to the exact value of the integral. In particular, Fig. 3 shows the average minimum residual over a range of source positions, y , between the intensity computed by either the perturbative expansion or the geometric/Eikonal approximation with the exact value of the intensity as a function of ν and κ . That is, we define the residual to be

$$\text{Res} = \frac{1}{2L} \min \left[\int_{-L}^L |F^{\text{pert.}}(y)|^2 - |F(y)|^2 dy, \int_{-L}^L |F^{\text{geom.}}(y)|^2 - |F(y)|^2 dy \right] / \max_{-L \leq y \leq L} (|F(y)|^2), \quad (15)$$

where we normalize the residual by the maximum value of the intensity. The exact intensity is computed using Picard-Lefschetz theory, as described in Appendix A. The residual is small when one of the approximations is valid, and becomes large when neither is valid. Note that the geometric/Eikonal approximation diverges for a small region around caustics. To avoid this divergence, we choose $L = \frac{3}{4}y_c$, where y_c is the location of the fold caustic. That is, for the rational lens, when $\kappa > \frac{1}{2}$, the lens exhibits a caustic at $y = \pm y_c$ where $y_c = \frac{3\sqrt{3}}{8}\kappa$ for large κ . Since most of the flux is contained within the region $-y_c < y < y_c$, we choose L such that we are within this region, in order to avoid the caustics. For $\kappa \leq \frac{1}{2}$, we choose $L = 2$.

Fig. 3 shows the residual computed in this way as a function of κ and $\epsilon = \kappa\nu$. From the residual, we can see that both approximations fail at $\epsilon = 1$, which is shown as the red, dashed line. As ϵ decreases, the diffractive/perturbative approximation becomes valid, whereas when ϵ increases, the geometric approximation becomes valid. Thus, the line $\epsilon = 1$ forms a boundary between the regimes

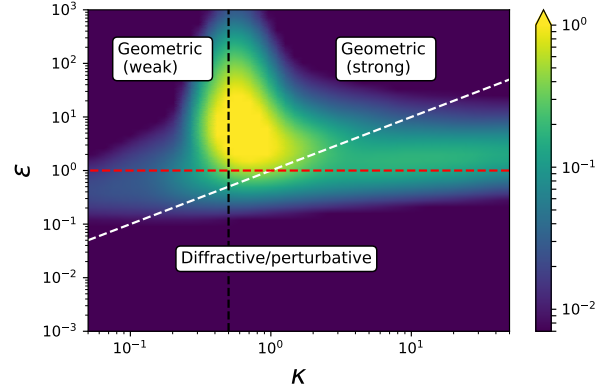


Figure 3. The minimum average residual between the exact value of the intensity of the Kirchhoff-Fresnel integral (computed using Picard-Lefschetz theory) with the perturbative expansion or geometric/Eikonal approximation over a range of source positions, y . This residual is defined explicitly in Eq. (15). For $\kappa > 1/2$, we choose $L = y_c$, where y_c is the location of the fold caustic. For $\kappa < 1/2$, we choose $L = 2$. The residual is shown as a function of κ and $\epsilon = \kappa\nu$. The regions are labelled according to the approximation which minimizes the residual. The labels “strong” and “weak” refer to the strong and weak lensing regimes discussed in Section 4 and corresponding to Table 1. The red, white, and black dashed lines correspond to the lines $\epsilon = 1$, $\nu = 1$, and $\kappa = 1/2$, respectively.

of validity of these two approximations. This suggests that ϵ is the appropriate scale that determines when geometric optics holds, as opposed to the Fresnel scale which only depends on the frequency ν . The $\nu = 1$ line is shown as the white, dashed line. If, indeed, the Fresnel scale were the appropriate separation scale, one would expect the geometric approximation to always hold above this line, and always fail below it. This is clearly not the case, however, as for small κ , the geometric approximation appears to fail even when $\nu > 1$, and for large κ it can remain valid for $\nu < 1$.

Fig. 3 also highlights the boundary at $\kappa = 1/2$, which is where the cusp caustic occurs. The cusp occurs when the two fold caustics merge, and $y_c \rightarrow 0$. The increase in the residual around this line is due to the fact that as $y_c \rightarrow 0$, our selection of the range $-y_c < y < y_c$ no longer avoids the caustics. Note, however, that as ϵ increases, the region around the caustic for which the geometric/Eikonal approximation diverges becomes smaller. We label the two regions to the left and right of $\kappa = 1/2$ weak and strong geometric optics, respectively, as it is only when $\kappa > 1/2$ that multiple real images are formed by the lens, as we discuss further in Section 4.

Fig. 4 further examines the transition from the geometric regime to the diffractive/perturbative regime by comparing the asymptotic behaviour of the exact Kirchhoff-Fresnel integral, the perturbative expansion, and the geometric/Eikonal approximation as a function of frequency for specific values of κ and y . Five values of κ and y were chosen, corresponding to the five distinct regions discussed in Appendix A. In short, these five regions correspond to the five distinct Lefschetz thimble topologies for this lens, or, in other words, each region has a unique number of real and relevant complex images. What is shown in Fig. 4 is not the total intensity, $|F(y)|^2$, but rather the absolute value squared of the total wave-field minus one, $|F(y) - 1|^2$. This way we are comparing the value of the asymptotic scaling of the perturbative part in the diffractive regime. The exact value, computed using Picard-Lefschetz theory, is shown

in blue, whereas the perturbative expansion and geometric optics results are shown in purple and green, respectively.

As expected, regardless of the choice of source position and lens strength, the geometric limit returns the correct asymptotic behaviour for large frequencies (except at caustics), whereas the perturbative/diffractive limit assumes the correct asymptotic behaviour for low frequencies. What is notable, however, is that the frequency where this transition occurs depends on the lens strength κ , and, in particular, is given to an order-of-magnitude by $\epsilon = 1$. In the region where both approximations agree with each other (around $\epsilon = 1$), neither approximation agrees with the true result, but unlike with small frequencies, where geometric optics is off by orders-of-magnitude, and large frequencies, where the perturbative expansion is off by orders-of-magnitude, both are only off by a few factors of unity. It is particularly striking that for large lens strengths, the geometric approximation can hold for very low frequencies (for example, when $\kappa = 5,000$ and $y = 1000$, geometric optics holds down to $\nu \sim 10^{-3}$). Similarly, when κ is small, geometric optics can be made to fail for large frequencies (when $\kappa = 0.25$ and $y = 0$, the geometric approximation fails as early as $\nu \sim 10$).

We infer two things from these results. First, that, together, geometric optics and the perturbative expansion can be used to accurately describe most of parameter space, except for a small region where they overlap. Secondly, the quantity that determines the separation between these two regimes is $\epsilon = \kappa\nu$, as opposed to the Fresnel scale. Expressed in terms of dimensionful quantities, $\epsilon = \kappa a^2 / R_F^2$, where a is the size of the lens (see Section 6). Thus, the physical scale that separates the diffractive and refractive regimes is given by $R_F / \sqrt{\kappa}$ (i.e. when the size of the lens is much larger than this scale, refractive optics holds, and when it is much smaller, diffractive optics holds). This means that the convergence plays an important role in determining whether geometric optics holds, rather than the frequency alone. Thus, the simple heuristic that geometric optics is valid when the wavelength is small compared to the size of the lens is generically false.

4 STRONG SCINTILLATION IN THE REFRACTIVE AND DIFFRACTIVE REGIMES

The result of the previous section suggests that it cannot always be taken for granted that short wavelengths automatically mean geometric optics holds. Rather, one must also know the lens strength, or convergence, in order to assess whether one is in the geometric or diffractive regime. At first glance, this seems like a challenge, as the convergence is a much more difficult quantity to measure. However, in this section, we will make a simple scaling argument that an observation of large flux variations implies that the lensing is taking place in the geometric regime. In other words, diffractive lensing is typically weak. Thus, for many practical purposes (e.g. pulsar scintillation and extreme-scattering events), any lensing observations are likely to occur in the geometric optics regime. It is possible to define strong versus weak lensing in many ways; however, in order to make a simple scaling argument, here we will consider lensing to be strong when most of the flux is localized to some finite region in the observer plane (as opposed to being diffuse across the observer plane). We will again study the simple rational lens to make our argument, and we will consider four limiting cases: when $\kappa \gg 1$ and $\kappa \ll 1$, with $\epsilon \gg 1$ or $\epsilon \ll 1$.

As we have shown, when $\epsilon \gg 1$ we are in the geometric regime and when $\epsilon \ll 1$ we are in the diffractive or perturbative regime. In either case, outside of a certain region centred around the origin, the

intensity above unity, $|F|^2 - 1$, falls off exponentially. This is easy to see for the perturbative/diffractive regime from Eq. (10). This is a little more difficult to see for geometric optics, but as we show in Appendix A, for any κ there exists a y beyond which the only relevant images are a single real image and one or two imaginary images. The real image is effectively unperturbed and has an intensity of order unity, and the imaginary images have an intensity that has an exponential dependence on the impact parameter that goes like $e^{-i\nu y}$. Thus, in both the geometric and diffractive regimes there is a region in the observer plane (with an area we will call σ) outside of which the intensity decays exponentially. We will consider the lensing to be strong if the total rms intensity variations in this region is of order unity or larger. If this is not the case, then most of the displaced flux is in the exponentially damped region and we consider this to be weak lensing. Fig. 5 shows an illustrative example computed for $\kappa = 5$ and $\nu = 2$ in the geometric regime. Outside of a region of width σ , the intensity peaks decay exponentially, and the rms intensity fluctuations within the region are given by μ . The total rms fluctuations are then given by $m = \sigma\mu$, which is sometimes referred to as the scintillation index. The lensing is considered weak when $m \ll 1$.

First, let us consider $\kappa \gg 1$. If $\epsilon \gg 1$, then we are in the geometric regime. Since $\kappa > 0.5$, the value of σ is set by the region between the two caustics (see Fig. A1). For $\kappa \gg 1$, the area between the caustics scales as $\sigma \sim \kappa$. Now, when κ is large, using Eq. (13) and Eq. (4), the intensity fluctuations, which we will call μ , are of order $\sim \kappa^{-1}$. Thus, the total rms fluctuations are $m = \sigma\mu \sim 1$, which we consider strong lensing. When $\epsilon \ll 1$, we are in the perturbative/diffractive regime. From Eq. (10), the cross section is given by $\sigma \sim \nu^{-1}$, and the intensity fluctuations are $\mu \sim \epsilon^2\nu$. Thus, in this regime, $m = \sigma\mu \sim \epsilon^2 \ll 1$. So, when κ is large, strong lensing is never described by the perturbative or diffractive regime.

Now, if $\kappa \ll 1$, there are no caustics. Thus, for $\epsilon \gg 1$ (the geometric regime), the cross section is given by the width of the exponential decay of the intensity of the imaginary images, which is $\sigma \sim \nu^{-1}$. Expanding the intensity fluctuations in the geometric limit in terms of κ , we obtain that the intensity fluctuations are $\mu \sim \kappa$. Thus, the total rms fluctuations are $m = \sigma\mu \sim \kappa/\nu \ll \kappa^2 \ll 1$, since $\epsilon = \kappa\nu \gg 1$. When $\epsilon \ll 1$ (the perturbative regime), we have again that $\sigma \sim \nu^{-1}$ and $\mu \sim \epsilon\nu$, so $\sigma\mu \sim \epsilon$. Thus, when $\kappa \ll 1$, regardless of whether we are in the refractive or diffractive regime, the lensing is weak.

Table 1 summarizes these results. We have argued that strong lensing generally occurs when $\kappa \gg 1$ and $\epsilon \gg 1$, but not when either $\kappa \ll 1$ or $\epsilon \ll 1$. In other words, any lensing described by the perturbative or diffractive regime is weak. Another way to make this argument is to look at the peak intensity value for the perturbative expansion, which occurs when $y = 0$; in particular, $|F^{\text{pert.}}(0) - 1|^2 \sim \epsilon^2\nu = \kappa^2\nu^3$. In order for this to be of order unity or larger and for the perturbative expansion to hold, we require $\kappa^2\nu^3 \gtrsim 1$ and $\kappa\nu \ll 1$, which together imply that $\nu \gtrsim \kappa^{2/3}$ and $\kappa^{1/3} \ll 1$. Thus, the maximum intensity fluctuations are only ever larger than unity in the perturbative regime in a small region of parameter space when the lens strength κ is small. This has implications for plasma lensing observations, as it suggests that strong diffractive interstellar scintillation (sometimes referred to as DISS in the plasma lensing literature) may never be a good description. In other words, extrapolating the perturbative expansion to strong lensing regimes may generically lead to an incorrect description of the lensing phenomenon. We discuss the implications for plasma lensing further in Section 6.

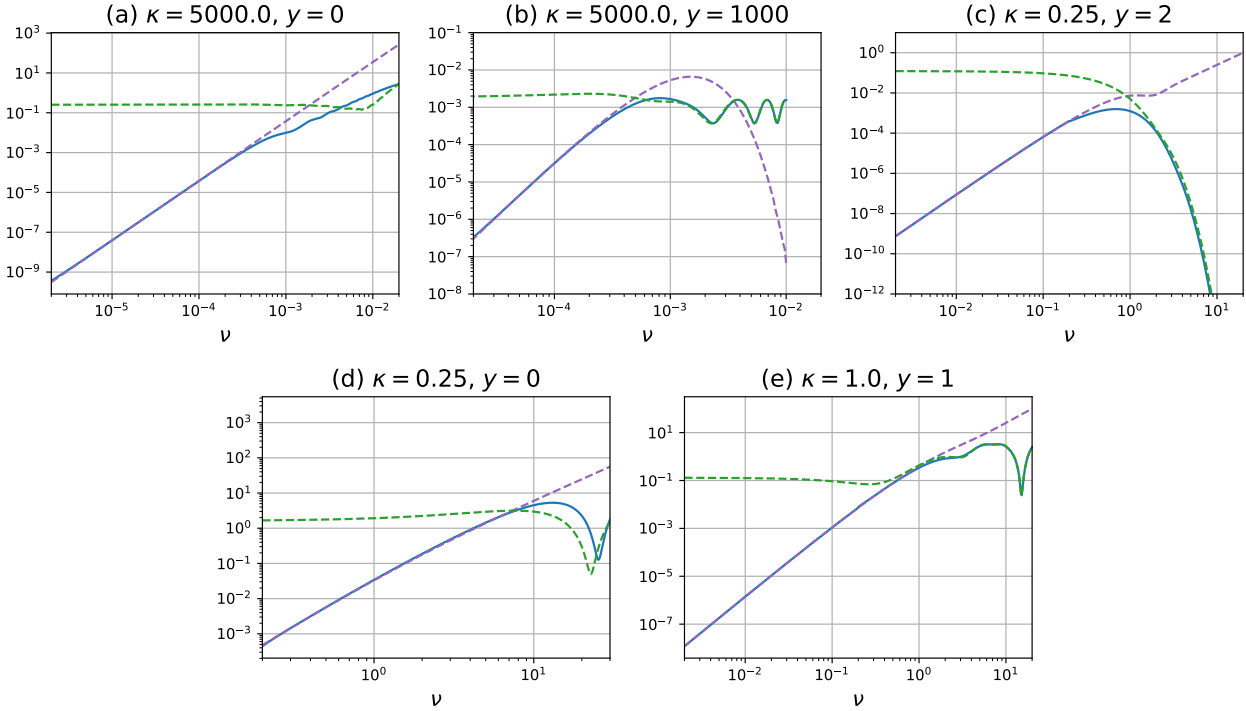


Figure 4. Comparison of the absolute value of the wave-field minus one, $|F(y) - 1|^2$, as a function of frequency for the perturbative/diffractive expansion (dashed purple lines), geometric optics (dashed green lines), and the exact evaluation of the Kirchhoff-Fresnel integral computed using Picard-Lefschetz theory (blue). The curves are computed for five different values of κ and y , which correspond to values in the five topologically distinct regions of the rational lens shown in Fig. A1.

κ	$\epsilon = \kappa\nu$	regime	cross section (σ)	intensity fluctuations (μ)	$m = \sigma\mu$	strong/weak
$\gg 1$	$\gg 1$	geometric / refractive	$\sim \kappa$	$\sim \kappa^{-1}$	~ 1	strong
$\gg 1$	$\ll 1$	perturbative / diffractive	$\sim \nu^{-1}$	$\sim \epsilon^2 \nu$	$\sim \epsilon$	weak
$\ll 1$	$\gg 1$	geometric / refractive	$\sim \nu^{-1}$	$\sim \kappa$	$\ll \kappa^2$	weak
$\ll 1$	$\ll 1$	perturbative / diffractive	$\sim \nu^{-1}$	$\sim \epsilon^2 \nu$	$\sim \epsilon$	weak

Table 1. Summary of the scaling arguments for the strength of lensing in the different regimes for the simple rational lens. Strong lensing never occurs when $\kappa \ll 1$, or when the perturbative expansion holds.

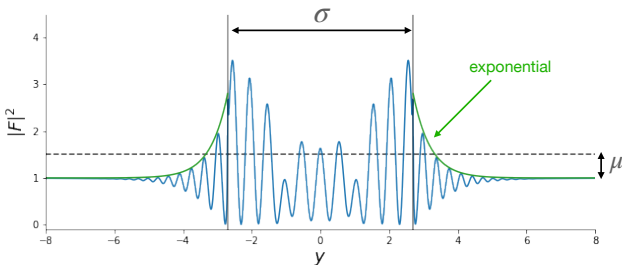


Figure 5. Intensity fluctuations as a function of y for the rational lens with $\kappa = 5$ and $\nu = 2$. Outside of a region of width σ , the intensity fluctuations decay exponentially. Within the region, the intensity fluctuations have an rms of μ .

5 MEASURING TIME DELAYS

In the previous section, we argued that strong scintillation generically occurs in the geometric regime, whereas diffractive optics generically produces weak scintillation, as the total rms intensity

fluctuations only becomes of order unity in the geometric regime. However, while the total rms fluctuations may increase, even if the intensity fluctuations are large (especially near caustics), if the resolution of an observation is too small, the actual observed intensity fluctuations will be washed out. In particular, in geometric optics, when $\kappa \gg 1$, the average fluctuations are $\mu \sim \kappa^{-1} \ll 1$. Thus, even when the lensing is described by multiple geometric images, it may still appear to be weak. How then are we to distinguish geometric optics from diffractive/perturbative optics in such a scenario? Fortunately, the two regimes behave qualitatively very distinctly in delay space.

Observationally, the quantity one typically observes is the wave-field as a function of frequency and time, $F(\nu, t)$, where the time dependence comes from the relative motion of the source and lens as a function of time, $y(t)$. Here we will focus on the wave-field as a function of frequency. Typically, one actually observes the dynamic spectrum, which is the intensity, $|F|^2$, as a function of frequency and time; however, novel phase retrieval techniques have made observations of the underlying wave-field possible (Spencer et al. 2021).

Consider lensing in the geometric regime when multiple images are present. Then the wave-field takes the form

$$F^{\text{geom.}}(\nu) = \sum_j \frac{1}{|\Delta_j|^{1/2}} e^{iS(x_j, y; \nu, \kappa) - i \frac{\arg(\Delta_j)}{2}}, \quad (16)$$

as in Eq. (4). Now, consider taking a Fourier transform of the wave-field as a function of frequency. In the geometric regime, the result is

$$\hat{F}_\nu \propto \sum_j \frac{1}{|\Delta_j|^{1/2}} \delta(\tau - T(x_j, y, \kappa)), \quad (17)$$

where \hat{F}_ν denotes the Fourier transform of F as a function of ν , τ is the conjugate variable of ν , and $T(x, y, \kappa) \equiv \frac{1}{2}(x - y)^2 + \kappa\psi(x)$ is the dimensionless time-delay associated with an image at x . Thus, in the geometric regime, the wave-field in delay space is a sum of delta functions centred at well-defined time delays associated with each image. Conversely, as we argue in Appendix A, in the low-frequency limit, the geometric images become mutually coherent, so that the diffractive/perturbative wave-field, rather than being characterized by an interference pattern of multiple incoherent images, effectively becomes a single image with a small modulation on top. Thus, one would not expect the diffractive/perturbative wave-field to exhibit distinct images in delay space.

Fig. 6 shows the intensity fluctuations and the conjugate wave-field, \hat{F}_ν , for the rational lens with $\kappa = 1000$ and $y = 162$, which is halfway to the caustic ($y = y_c/2$). The lensing is computed for three different frequency ranges, $\nu \in [0, 0.002]$, $[0, 0.01]$, and $[0, 20]$, where the ranges are chosen so that the lensing occurs firmly in the diffractive/perturbative regime for the smallest range, firmly in the geometric/Eikonal regime for the largest range, and neither for the intermediate range.

For the choice of κ and y , there are four relevant images: three real, and one imaginary. In other words, the sum in Eq. (16) contains four terms, where x_j is purely real for three of those terms. As a result, the conjugate wave-field for the geometric regime (the top panel) is, in principle, a sum of four delta functions. Due to the finite bandwidth, $\Delta\nu$, for which we calculate the wave-field, the conjugate wave-field for the geometric regime is actually given by $|F_\nu|^2 \sim \sum_j (\tau - T(x_j))^{-2}$. The right column of Fig. 6 shows the amplitude of the conjugate wave-field normalized by the frequency bandwidth, $|F_\nu/\Delta\nu|^2$. Under this normalization, the amplitude of the individual peaks (in the geometric regime) are exactly given by $|\Delta_j|^{-1}$. Thus, under this normalization, the height of the peaks in delay space give the amplitude of the geometric images, and the location of the peaks give the time delay associated with each image. Note that the top-right panel of Fig. 6 only shows the peaks associated with two of the four images. In geometric optics, the imaginary part of x_j for the complex image causes the amplitude to be exponentially suppressed, and so its contribution to the total power is negligible compared to the other images. The other real image is the “unperturbed” image centred at $\tau = 0$, with $|\Delta_j|^{-1} = 1$. The top-right panel of Fig. 6 zooms in on the lensed images so that they are easily resolvable by eye. Both of these images have amplitudes of $|\Delta_j|^{-1} \sim \kappa^{-1} \sim 10^{-3}$. Thus, while the intensity fluctuations shown in the top-left panel may be much larger, ~ 0.2 , when the oscillations are averaged over (as might occur for an observation with limited frequency resolution), the observed fluctuations could potentially be as small as 10^{-3} .

As we describe in Appendix A, one of the main conceptual advantages of using Picard-Lefschetz theory to evaluate the Kirchhoff-Fresnel integral is that even for low-frequencies, one can separate

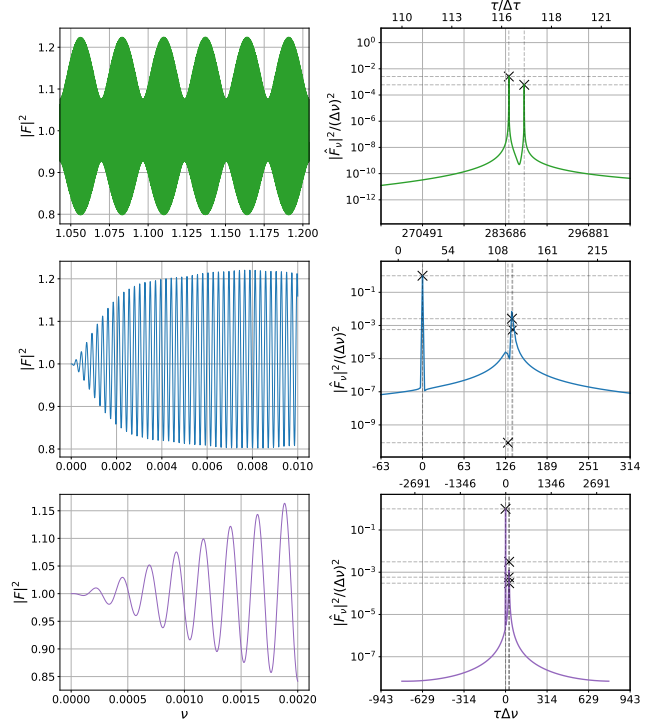


Figure 6. (Left column) The intensity $|F(\nu)|^2$ of the rational lens computed for $\kappa = 1000$ and $y = 162$, for different ranges of frequency, ν . The frequency ranges are chosen such that the top panel occurs firmly in the geometric regime ($\epsilon = \kappa\nu \gg 1$), the bottom panel occurs in the perturbative regime ($\epsilon < 1$), and the middle panel occurs in an intermediate regime. (Right column) The Fourier transform of the wave-field as a function of ν , denoted by $\hat{F}_\nu(\tau)$, where τ is the conjugate variable of ν . The vertical axis shows $|\hat{F}_\nu/\Delta\nu|^2$ where $\Delta\nu$ is the frequency bandwidth for which the wave-field was computed. Under this normalization, the conjugate wave-field in the geometric optics regime is a sum of isolated peaks centred at the time delay for each image, with a height given by the individual intensity of the image in the geometric optics approximation. The black X's in the right column correspond to each of the images' individual intensities and time delays. Picard-Lefschetz theory makes it possible to assign individual intensities to the relevant images even at small frequencies. The horizontal axis of the left column is shown in two units: units of the fundamental delay resolution given by $(\Delta\nu)^{-1}$, and units of the relative time delay $\Delta\tau$, which is the distance between the two peaks shown in the top right panel.

the integral into contributions from a discrete set of images that correspond to the geometric limit as one increases the frequency. The height of the black X's in the right column of Fig. 6 correspond to the amplitude of each of the relevant images computed using Picard-Lefschetz theory, shown at the corresponding time delay. In particular, one can see that while the imaginary image is exponentially suppressed in geometric optics, and thus not shown on the top-right panel, as the frequency decreases, the imaginary image becomes significant, and indeed has an amplitude comparable to the real images in the bottom panel.

Now, while separating the wave-field into distinct contributions from the relevant images is a mathematically well-defined procedure under Picard-Lefschetz theory, we can see that the form of the conjugate wave-field in delay space is qualitatively very different between the geometric and diffractive/perturbative regimes. Specifically, the conjugate wave-field for the perturbative regime is no longer a simple sum of delta functions. While, regardless of

frequency, there is always a peak centred at $\tau = 0$ and with height of unity corresponding to the unperturbed image (which always must be present even in the absence of a lens), the lensed images cease to form well-defined peaks in delay space, and instead merge into a single peak with some width. The width of this merged peak increases as the frequency decreases.

Another way to think of this is by considering two fundamental time-scales in delay space. First, there is the resolution scale given by $(\Delta\nu)^{-1}$. That is, the maximum resolution in the variable τ for which one can compute the conjugate wave-field is given by the inverse of the bandwidth over which one observes the wave-field itself. The second time-scale one may consider is the relative delay between the lensed images. Consider the two real images (aside from the un-perturbed image), which we will call x_1 and x_2 . Then this relative delay is $\Delta\tau \equiv |T(x_1) - T(x_2)|$. This delay between the lensed images can be thought of as the effective geometric width of the lens in delay space.

The conjugate variable τ , scaled by both of these time-scales, is shown in Fig. 6, with the values of $\tau\Delta\nu$ being shown on the bottom horizontal axis, and the values of $\tau/\Delta\tau$ shown on the top horizontal axis. Note that geometric optics corresponds to the regime when $\Delta\tau \ll (\Delta\nu)^{-1}$. Conversely, the perturbative regime occurs when $\Delta\tau \gg (\Delta\nu)^{-1}$. This can be easily made sense of when we realize that for large κ , we have $\Delta\tau \sim \kappa$. Thus, $\Delta\tau \sim (\Delta\nu)^{-1}$ when $\epsilon \sim \kappa\Delta\nu \sim 1$. In other words, geometric optics is obtained in the limit where the fundamental resolution limit in delay space is much smaller than the relative time delays of the lensed images. Diffractive/perturbative optics occurs when the relative time delays become smaller become un-resolvable in the conjugate wave-field. Observationally, this leads to a rather straightforward way of diagnosing whether or not an observation occurs in the geometric or diffractive regime, since it is often possible to measure the relative time delays of scattered images.

6 IMPLICATIONS FOR TURBULENT PLASMA LENSING

In this section we will discuss the implications of our results for the study of plasma lensing. Following observations of extreme scattering events (ESEs) in pulsars (Fiedler et al. 1987) and the discovery of pulsar scintillation (Scheuer 1968; Rickett 1977), both of which are thought to be due to scattering in the interstellar medium (ISM), there has been significant effort to understand wave effects in plasma lensing. The expectation that fast radio bursts (FRBs) will be lensed in a similar way to pulsars has increased the need for a robust understanding of wave optics in lensing.

Due to the difficulties in computing the Kirchhoff-Fresnel integral, studies of strong plasma lenses typically restrict their attention to geometric optics, especially in the case of studies attempting to model ESEs (see e.g. Romani et al. 1987; Clegg et al. 1998; Pushkarev et al. 2013; Bannister et al. 2016, 2019). Studies of pulsar scintillation have also included studies of the diffractive interstellar scintillation phenomenon (DISS), for which the perturbative expansion of the Kirchhoff-Fresnel integral is assumed to hold (see e.g. Wang et al. 2005; Lewandowski et al. 2011; Dai et al. 2016). Much of our understanding of when the different regimes of wave optics in plasma lensing comes from an earlier effort to develop the theory of turbulent plasma lensing (Lee & Jokipii 1975; Prokhorov et al. 1975; Blandford & Narayan 1985; Goodman & Narayan 1985; Cordes et al. 1986; Codona et al. 1986; Cordes & Rickett 1998). Rickett (1990) reviews much of this earlier theoretical work, the

results of which are also presented in the textbook, The Handbook of Pulsar Astronomy (Lorimer & Kramer 2012), which is widely referred to in the pulsar astronomy community. These early works on turbulent plasma lensing relied on approximation schemes for the Kirchhoff-Fresnel integral, which, in the absence of a robust method for evaluating oscillatory integrals exactly, were assumed to hold based on heuristic arguments, rather than explicit quantitative validation. The results we have presented here for a simple lens model suggest that these previous works may have overestimated the applicability of these approximations in certain regimes.

In order to compare our results with the turbulent plasma lensing literature, we will first re-write the Kirchhoff-Fresnel integral using the dimensionful parameters that appear in plasma lensing. Eq. (1) becomes

$$F(y) \propto \int \exp \left\{ i \frac{\omega}{c} \left[\frac{(\hat{x} - \hat{y})^2}{2} + \frac{\bar{d} c e^2 \Sigma_e(\hat{x})}{2 m_e \epsilon_0 \omega^2} \right] \right\} d\hat{x}, \quad (18)$$

where ω is the angular frequency of the source radiation, $\bar{d} = d_{sI}d_I/d_s$ is the reduced distance, $\hat{y} = (\hat{x}_s d_I + \hat{x}_o d_{sI})/d_s$ is a weighted average of the transverse displacement of the source and observer, and Σ_e is the projected electron column density of the plasma in the lens plane. Fig. 1 shows the distances and the coordinates involved in this parametrization.

Now, in order to compare this with our dimensionless analysis, we re-scale the coordinates by a , which we take to be the size of the lens. That is, we take $\hat{x} \rightarrow x = \hat{x}/a$, $\hat{y} \rightarrow y = \hat{y}/a$, and $\Sigma_e(\hat{x}) \equiv \Sigma_0 \psi(x)$, where a is defined so that $\psi''(0) \approx -2$. Defined in this way, Σ_0 is the amplitude of the plasma surface density variation. Thus, Eq. (18) reduces to Eq. (1), with

$$\nu = \frac{\omega a^2}{c \bar{d}} = \frac{a^2}{R_F^2}, \quad (19)$$

$$\kappa = \frac{\bar{d} e^2 \Sigma_0}{2 a^2 m_e \epsilon_0 \omega^2}, \quad (20)$$

where $R_F \equiv (\lambda \bar{d}/2\pi)^{1/2}$ is the dimensionful Fresnel scale. Thus, as we stated before, the condition that ν be large is equivalent to the Fresnel scale being small relative to the size of the lens. For plasma lensing, we obtain

$$\epsilon = \frac{e^2 \Sigma_0}{2 m_e c \epsilon_0 \omega}. \quad (21)$$

Note that since the convergence scales with the inverse frequency squared in plasma lensing, we have $\epsilon \sim \omega^{-1}$. Thus, geometric optics ($\epsilon \gg 1$) is obtained in the low frequency limit, and diffractive optics ($\epsilon \ll 1$) in the large frequency limit.

The primary difficulty in comparing our results to the previous literature is that much of the study of wave optics in plasma lensing was performed for turbulent lenses. That is, whereas we consider a smooth $\psi(x)$ with a single peak, studies of turbulent plasma lensing consider a Gaussian random field as the lensing potential. As a result, the primary goal of these calculations is not to compute the observed light curve for a particular lens, but to compute the statistical properties of the electric field at the observer given some power spectrum defining the lens. For example, Rickett (1990) reviews the study of turbulent plasma lenses with power spectra of the form

$$P(k) \propto (k^2 + k_{\text{outer}}^2)^{-\beta/2} \exp(-k^2/k_{\text{inner}}^2). \quad (22)$$

Between the inner and outer scales set by k_{inner} and k_{outer} , this power spectrum is a simple power law, $P(k) \propto k^{-\beta}$, and, in particular, is Kolmogorov for $\beta = 11/3$. Outside of these scales, the power spectrum falls rapidly to zero.

The early work on turbulent plasma involved approximating the Kirchhoff-Fresnel integral using perturbative methods, in addition to the Eikonal or stationary phase approximation (see e.g. Prokhorov et al. 1975), as exact methods for computing the diffraction integral were not generally available. Naturally, these works were concerned with the delineation of the regimes of applicability of these approximation schemes. One of the main results of this early work, summarized in Rickett (1990) and Lorimer & Kramer (2012), was the perturbative computation of the observed intensity fluctuations for a power spectrum of the form of Eq. (22). It was found that the intensity fluctuations were much less than unity when the Fresnel scale was larger than the coherence scale, s_0 , which is defined as the average lateral separation in the observing plane across which there is a one-radian difference in phase calculated along a straight line path from source to observer. Conversely, when the coherence scale is larger than the Fresnel scale, the intensity fluctuations predicted by the perturbative calculation exceed unity. Thus, a quantity can be defined

$$u = \frac{R_F}{s_0}, \quad (23)$$

such that when $u < 1$ the amplitude of the intensity fluctuations predicted by the perturbative expansion are weak and when $u > 1$ they are strong (Rickett 1990).

For $u < 1$, which was taken to be the weak lensing regime, the perturbative expansion was assumed to hold. The strong lensing regime ($u > 1$) was further split into the diffractive and refractive regimes, where diffraction occurs on small scales and refraction occurs on large scales. The scales at which these regimes occurred were determined by the following heuristic arguments, which can be found in Rickett (1990) and Lorimer & Kramer (2012).

From the definition of the coherence scale, s_0 , one can define the diffractive scattering angle, $\theta_d \sim \lambda/s_0$, which is roughly the average bending that light rays undergo as they pass through the plasma (Salpeter 1967; Rickett 1990). If we consider the electric field at the observer to be a sum of point sources located along the lens (the Huygens-Fresnel principle), then the observed diffractive intensity variations come only from the waves within the angular spectrum of width θ_d . When the observer is laterally displaced by s_0 , the relative phase of the incoming waves are substantially shifted from the original observer position (by roughly one radian), resulting in significant differences in the observed intensity across this scale. Thus, the diffractive scale, s_d , is taken to be roughly equal to the coherence scale, $s_d \approx s_0$. Now, intensity variations due to refraction (i.e. due to the bending of multiple light rays into the line of sight of the observer) must occur on scales larger than $s_r = \bar{d}\theta_d$. This is because two observers separated by a distance less than $\bar{d}\theta_d$ will have overlapping scattering disks. Thus, any significant intensity variations on scales larger than this must be due to multiple images being refracted into the line of the sight of the observer. Fig. 7 shows a diagram to help visualize this picture of turbulent scattering.

Altogether, in terms of the Fresnel scale and u , one can write the diffractive and refractive scales as (Rickett 1990; Lorimer & Kramer 2012)

$$s_r = uR_F, \quad (24)$$

$$s_d = \frac{R_F}{u}. \quad (25)$$

Fig. 8 summarizes this picture of turbulent plasma lensing that arises from this description. When $u < 1$, the intensity fluctuations are weak and the perturbative expansion holds. When $u > 1$, the

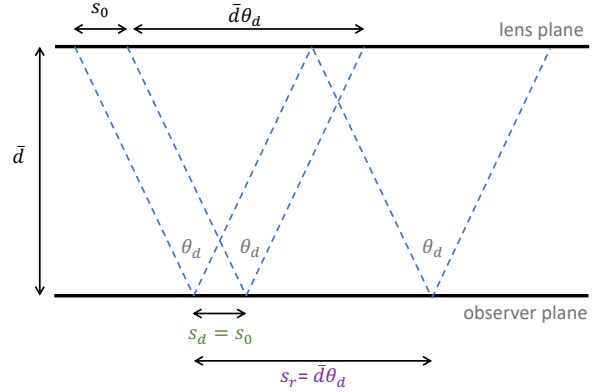


Figure 7. Diagram of the turbulent plasma scattering picture. Diffractive intensity variations at an observer come from waves emanating from within a scattering angle of θ_d . The diffractive scale, s_d , is taken to be roughly equal to the coherence scale, s_0 , which is the average lateral distance over which the phase along a straight line path from source to observer varies by one radian. The refractive scale, s_r , is taken to be $\bar{d}\theta_d$, as observers separated by larger than this have no overlap between their scattering disks.

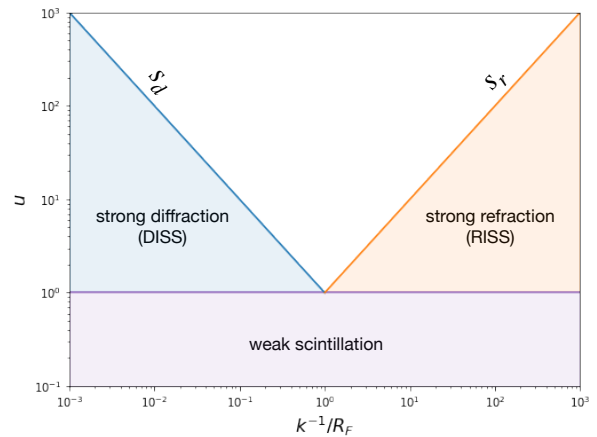


Figure 8. Summary of the regimes described in early turbulent plasma lensing literature. The statistics of the observed electric field is taken to be described by diffractive interstellar scattering (DISS) for spatial scales less than $s_d = R_F/u$ and by refractive interstellar scattering (RISS) for spatial scales greater than $s_r = uR_F$. The quantity u plotted on the y-axis sets the predicted strength of the diffractive intensity variations, where they are much less than unity for $u < 1$ and greater than unity for $u > 1$. The x-axis is the spatial scale of intensity variations k^{-1} normalized by the Fresnel scale. Note that this description is in contrast with our lens model, for which the refractive regime can be made to hold at arbitrarily small scales when the lens strength is large.

intensity fluctuations are split into distinct diffractive and refractive regimes. The Fresnel scale sets the boundary between diffractive and refractive lensing, but as u gets large, the region around the Fresnel scale for which neither approximations hold gets larger. Fig. 1 of Rickett (1990), which shows a schematic of the power spectrum of the observed intensity fluctuations as a function of scale, also presents this picture of lensing where the Fresnel scale sets the boundary between two distinct regimes.

Our results, however, are at odds with this picture. Firstly, we

find that, for the rational lens, rather than the Fresnel scale setting the transition point between diffractive (perturbative) and refractive (geometric) optics, the dimensionless parameter $\epsilon = \kappa\nu$ does. In particular, if the lens strength is large, geometric optics may hold well below the Fresnel scale, and likewise if it is small, it may fail at arbitrarily large scales. Secondly, we find that even when the intensity variations are small, the perturbative expansion may still fail. See, for example, panel (b) of Fig. 4, for which the perturbative expansion fails even while the intensity variations are of order $\sim 10^{-3}$. Likewise, large fluctuations predicted by the perturbative expansion do not necessarily indicate large fluctuations in the true value of the diffraction integral (see panel (c) of Fig. 4).

We also note that in Section 4, we argue that the condition for strong lensing to occur is that both $\kappa > 1$ and $\epsilon > 1$. In other words, whenever the perturbative expansion holds, the lensing is weak (though it need not be the case that weak lensing implies the perturbative expansion holds). This is in stark contrast with the definition of diffractive interstellar scintillation (DISS), which is taken to be the regime where lensing is both strong and described by a perturbative expansion. The study of DISS has led to attempts to infer physical properties from observations of pulsar scintillation, such as the spectral index of the ISM, the magnitude of electron density fluctuations, and the relative velocity of the observed pulsars (see e.g. Cordes & Rickett 1998; Wang et al. 2005; Lewandowski et al. 2011; Dai et al. 2016). If, as we have argued, perturbative calculations of the lensing phenomena are inappropriate for regimes of strong scintillation, then attempts to infer physical parameters using the framework of DISS may lead to biased results.

One prediction of this framework is that for a turbulent plasma with a lensing potential with Gaussian statistics, in the geometric optics limit, the intensity fluctuations of a scatter-broadened image are Gaussian, in the sense that as a function of the observation baseline, b , the intensity fluctuations scale as $\sim \exp\{-b^2\}$. Conversely, in diffractive optics, the intensity fluctuations are predicted to scale as $\sim \exp\{-b^{\beta-2}\}$, where β is the power-law index in Eq. (22). These predicted scalings of the intensity fluctuations have been used, for example, to separate diffractive and refractive regimes in interstellar scattering (see e.g. Johnson et al. 2018); however, the predicted Gaussianity of the refractive intensity fluctuations is based on the assumption that the refractive fluctuations only occur on scales where the lens potential is effectively smooth. Below this scale, it is assumed that diffractive/perturbative optics holds. However, we have argued that, depending on the amplitude of the lens, geometric optics may hold on scales much smaller than have previously been assumed. Thus, the particular scaling of intensity fluctuations may not be a strong indicator of the regime in which the lensing is occurring. Indeed, the Gaussian scaling of the intensity fluctuations and the regime of lensing may be entirely separate issues, though they have been conflated in the literature.

Of course, as mentioned previously, a straightforward application of our results to turbulent plasma lensing is challenging, as we have restricted our attention to a simple lens model. Due to the highly non-linear nature of the Kirchhoff-Fresnel integral, it is not immediately obvious that results for such a simple lens would be applicable to the more complicated case of turbulent lenses. Nevertheless, we feel that our description of the simple rational lens is in sufficient contrast to the description of lensing in the turbulent plasma lensing literature to warrant revisiting the theoretical basis of diffractive scintillation now that more robust tools for exactly evaluating the diffraction integral are available.

7 TYPICAL VALUES OF DIMENSIONLESS PARAMETERS

In this section, we compute the dimensionless parameters ν , κ , and ϵ for typical physical parameters that may occur in plasma lensing and gravitational lensing.

7.1 Plasma lensing

The study of wave optics in astrophysical plasma lensing is particularly relevant to pulsar observations, as pulsars are effectively coherent point sources. Pulsars are radio sources with frequencies of order GHz, and are found within the galaxy. Thus, we can expect typical distances to be $\bar{d} \sim 1$ kpc. Pulsars have been observed to undergo extreme scattering events (ESEs) due to lensing by roughly AU-scale features in the ISM, with excess electron column densities of order $\sim 0.01 \text{ pc cm}^{-3}$ (Coles et al. 2015; Kerr et al. 2018). Thus, using Eqns. 19 and 20, we obtain

$$\nu = 1.5 \times 10^4 \left(\frac{f}{1 \text{ GHz}} \right) \left(\frac{a}{1 \text{ AU}} \right)^2 \left(\frac{\bar{d}}{1 \text{ kpc}} \right)^{-1}, \quad (26)$$

$$\kappa = 100 \left(\frac{\Sigma_0}{0.01 \text{ pc cm}^{-3}} \right) \left(\frac{\bar{d}}{1 \text{ kpc}} \right) \left(\frac{a}{10 \text{ km}} \right)^{-2} \left(\frac{f}{1 \text{ GHz}} \right)^{-2}, \quad (27)$$

$$\epsilon = 1.5 \times 10^6 \left(\frac{\Sigma_0}{0.01 \text{ pc cm}^{-3}} \right) \left(\frac{f}{1 \text{ GHz}} \right)^{-1}. \quad (28)$$

Consistent with ESE observations, $\kappa \gg 1$, resulting in multiple real images and large intensity fluctuations. Moreover, we note that $\epsilon \gg 1$, suggesting that ESEs occur firmly in the geometric regime.

Note that the distance parameters \bar{d} and a both cancel out in the expression for ϵ . Thus, the factor which determines whether or not lensing occurs in the geometric or diffractive/perturbative regime depends only on the excess electron surface density and the frequency. In particular, we can use Eq. (28) to argue that pulsar scintillation generically occurs in the geometric regime, as $\epsilon \sim 1$ only occurs when the excess electron surface density is $\Sigma_0 \sim 10^{-8} \text{ pc cm}^{-3}$.

7.2 Gravitational lensing

In gravitational lensing, the surface mass density, as opposed to the electron column density, sets the amplitude of the lens potential. Moreover, the amplitude only depends on the surface mass density, and does not depend on frequency. In gravitational lensing, one is also often concerned with cosmological distances, and so the distances in $\bar{d} = d_{sl}d_l/d_s$ must be replaced by angular diameter distances, and the frequency ω must include include a redshift correction, $\omega \rightarrow (1+z)\omega$, where z is the redshift of the lens (Schneider et al. 1992). Otherwise, the formalism is exactly the same as plasma lensing.

We may wish to know the values of the dimensionless parameters in the case of lensing by a galaxy at cosmological distances. Thus, the lens has a size of order ~ 10 kpc and has a distance of order ~ 1 Gpc. Since fast radio bursts (FRBs) are the only coherent sources at cosmological distances, we will also be primarily concerned with radio frequencies. Given these typical parameters, the dimensionless frequency ν can be computed:

$$\nu \sim 6.5 \times 10^{16} (1+z) \left(\frac{f}{1 \text{ GHz}} \right) \left(\frac{a}{10 \text{ kpc}} \right)^2 \left(\frac{\bar{d}}{1 \text{ Gpc}} \right)^{-1}. \quad (29)$$

Many lens profiles have been used to model lensing by galaxies. One simple model is the Plummer model for which it is straightforward

to re-parametrize the convergence in terms of the total lens mass. One obtains that the convergence is given by $\kappa = 2GM\bar{d}/a^2c^2$ (Werner & Evans 2006).

$$\kappa \sim 1(1+z)^{-1} \left(\frac{M}{10^{12} M_{\odot}} \right) \left(\frac{\bar{d}}{1 \text{ Gpc}} \right) \left(\frac{a}{10 \text{ kpc}} \right)^{-2}. \quad (30)$$

Combining Eqs. 29 and 30, we obtain

$$\epsilon = 6.5 \times 10^{16} \left(\frac{M}{10^{12} M_{\odot}} \right) \left(\frac{f}{1 \text{ GHz}} \right), \quad (31)$$

which is generically much larger than unity.

8 CONCLUSION

Through the introduction of the mathematical framework of Picard-Lefschetz theory to the field of astrophysical lensing, it has now become possible to evaluate the Kirchhoff-Fresnel diffraction integral for a wide variety of situations. Previously, theoretical treatments of the study of wave optics in astrophysical contexts relied on various approximation schemes. Exact methods of computing diffraction integrals allow us to quantitatively evaluate longstanding assumptions in the field.

In this work, we have studied a simple lens model to assess when the perturbative approximation (diffractive optics) holds, and when the geometric limit of optics (refractive optics) holds. We find that, for the lens model we consider, there is no overlap in the regime of applicability of these two methods, and that the region of parameter space where neither method is valid is limited. That is optics is generically well described by either diffractive or refractive optics. We find that the spatial scale that separates these two regimes is given by the Fresnel scale divided by the square-root of the convergence, $R_F/\sqrt{\kappa}$. That is, for a lens with convergence κ and size a , refractive optics holds when a is larger than $R_F/\sqrt{\kappa}$, and diffractive optics holds when it is smaller. Previously, it has been assumed that the Fresnel scale alone sets the scale at which diffractive optics is valid. We have also argued that large intensity variations do not generically occur in the diffractive regime. This has important implications for the field of pulsar scintillometry.

In this work, we have focused on a simple, one-dimensional lens model. The highly non-linear nature of the Kirchhoff-Fresnel integral means that it is not straightforward to apply these results to more complicated lensing systems. Further detailed study of systems of interest, for example, turbulent plasma lensing, is needed. In particular, a similar analysis of the Gaussian random lens is a natural next step.

DATA AVAILABILITY

No new data were generated or analysed in support of this research.

ACKNOWLEDGEMENTS

We thank Fang Xi Lin for useful discussions. We receive support from Ontario Research Fund—research Excellence Program (ORF-RE), Natural Sciences and Engineering Research Council of Canada (NSERC) [funding reference number RGPIN-2019-067, CRD 523638-18, 555585-20], Canadian Institute for Advanced Research (CIFAR), Canadian Foundation for Innovation (CFI), the National Science Foundation of China (Grants No. 11929301), Thoth Technology Inc, Alexander von Humboldt Foundation, and the

Ministry of Science and Technology(MOST) of Taiwan(110-2112-M-001-071-MY3). Computations were performed on the SOSCIP Consortium’s [Blue Gene/Q, Cloud Data Analytics, Agile and/or Large Memory System] computing platform(s). SOSCIP is funded by the Federal Economic Development Agency of Southern Ontario, the Province of Ontario, IBM Canada Ltd., Ontario Centres of Excellence, Mitacs and 15 Ontario academic member institutions. Cette recherche a été financée par le Conseil de recherches en sciences naturelles et en génie du Canada (CRSNG), [numéro de référence 523638-18,555585-20 RGPIN-2019-067].

REFERENCES

- Bannister K. W., Stevens J., Tuntsov A. V., Walker M. A., Johnston S., Reynolds C., Bignall H., 2016, *Science*, **351**, 354, [arXiv:1601.05876](#)
- Bannister K. W., et al., 2019, *Science*, **365**, 565, [arXiv:1906.11476](#)
- Blandford R., Narayan R., 1985, *MNRAS*, **213**, 591
- Cherman A., Unsal M., 2014, arXiv e-prints, p. [arXiv:1408.0012](#), [arXiv:1408.0012](#)
- Clegg A. W., Fey A. L., Lazio T. J. W., 1998, *ApJ*, **496**, 253, [arXiv:astro-ph/9709249](#)
- Codona J. L., Creamer D. B., Flatté S. M., Frehlich R. G., Henyey F. S., 1986, *Journal of Mathematical Physics*, **27**, 171
- Coles W. A., et al., 2015, *APJ*, **808**, 113, [arXiv:1506.07948](#)
- Cordes J. M., Rickett B. J., 1998, *APJ*, **507**, 846
- Cordes J. M., Pidwerbetsky A., Lovelace R. V. E., 1986, *ApJ*, **310**, 737
- Cordes J. M., Wasserman I., Hessels J. W. T., Lazio T. J. W., Chatterjee S., Wharton R. S., 2017, *APJ*, **842**, 35, [arXiv:1703.06580](#)
- Dai S., Johnston S., Bell M. E., Coles W. A., Hobbs G., Ekers R. D., Lenc E., 2016, *MNRAS*, **462**, 3115, [arXiv:1607.07740](#)
- Er X., Wagner J., Mao S., 2022, *MNRAS*, **509**, 5872, [arXiv:2111.09104](#)
- Feldbrugge J., 2020, arXiv e-prints, p. [arXiv:2010.03089](#), [arXiv:2010.03089](#)
- Feldbrugge J., Turok N., 2020, arXiv e-prints, p. [arXiv:2008.01154](#), [arXiv:2008.01154](#)
- Feldbrugge J., Pen U.-L., Turok N., 2019, arXiv e-prints, p. [arXiv:1909.04632](#), [arXiv:1909.04632](#)
- Fiedler R. L., Dennison B., Johnston K. J., Hewish A., 1987, *Nature*, **326**, 675
- Goodman J., Narayan R., 1985, *MNRAS*, **214**, 519
- Gozzi E., Pagani C., Reuter M., 2021, *Annals of Physics*, **429**, 168457, [arXiv:2004.08874](#)
- Grillo G., Cordes J., 2018, arXiv e-prints, p. [arXiv:1810.09058](#), [arXiv:1810.09058](#)
- Johnson M. D., et al., 2018, *ApJ*, **865**, 104, [arXiv:1808.08966](#)
- Jow D. L., Foreman S., Pen U.-L., Zhu W., 2020, *MNRAS*, **497**, 4956, [arXiv:2002.01570](#)
- Jow D. L., Lin F. X., Tyhurst E., Pen U.-L., 2021, *MNRAS*, , [arXiv:2103.08687](#)
- Kerr M., Coles W. A., Ward C. A., Johnston S., Tuntsov A. V., Shannon R. M., 2018, *MNRAS*, **474**, 4637, [arXiv:1712.00426](#)
- Lee L. C., Jokiipii J. R., 1975, *ApJ*, **196**, 695
- Lewandowski W., Kijak J., Gupta Y., Krzeszowski K., 2011, *AAP*, **534**, A66, [arXiv:1107.3052](#)
- Lorimer D. R., Kramer M., 2012, *Handbook of Pulsar Astronomy*
- Main R., et al., 2018, *NAT*, **557**, 522, [arXiv:1805.09348](#)
- Nakamura T. T., Deguchi S., 1999, *Progress of Theoretical Physics Supplement*, **133**, 137
- Nye J. F., 1999, *Natural focusing and fine structure of light: caustics and wave dislocations*
- Pen U.-L., King L., 2012, *MNRAS*, **421**, L132, [arXiv:1111.6806](#)
- Prokhorov A. M., Bunkin F. V., Gochelashvili K. S., Shishov V. I., 1975, *IEEE Proceedings*, **63**, 790
- Pushkarev A. B., et al., 2013, *AAP*, **555**, A80, [arXiv:1305.6005](#)
- Rickett B. J., 1977, *ARA&A*, **15**, 479
- Rickett B. J., 1990, *ARA&A*, **28**, 561

- Romani R. W., Blandford R. D., Cordes J. M., 1987, *NAT*, **328**, 324
 Salpeter E. E., 1967, *APJ*, **147**, 433
 Scheuer P. A. G., 1968, *NAT*, **218**, 920
 Schneider P., Ehlers J., Falco E. E., 1992, *Gravitational Lenses*, doi:10.1007/978-3-662-03758-4.
 Shi X., Xu Z., 2021, *MNRAS*, **506**, 6039, arXiv:2104.00940
 Sprenger T., Wucknitz O., Main R., Baker D., Briske W., 2021, *MNRAS*, **500**, 1114, arXiv:2008.09443
 Tanizaki Y., Koike T., 2014, *Annals of Physics*, **351**, 250, arXiv:1406.2386
 Turok N., 2014, *New Journal of Physics*, **16**, 063006, arXiv:1312.1772
 Wang N., Manchester R. N., Johnston S., Rickett B., Zhang J., Yusup A., Chen M., 2005, *MNRAS*, **358**, 270, arXiv:astro-ph/0501218
 Werner M. C., Evans N. W., 2006, *MNRAS*, **368**, 1362, arXiv:astro-ph/0602368
 Witten E., 2010, arXiv e-prints, p. arXiv:1001.2933, arXiv:1001.2933
 Wright F. J., 1980, *Journal of Physics A: Mathematical and General*, **13**, 2913

APPENDIX A: PICARD-LEFSCHETZ ANALYSIS OF THE RATIONAL LENS

The purpose of this work has been to evaluate the regimes of validity of the refractive and diffractive regimes of optics through explicit comparison with the exact result of the Kirchhoff-Fresnel integral. In particular, we studied the simple rational lens, $\psi = 1/(1+x^2)$, as an example. Our ability to exactly compute the Kirchhoff-Fresnel integral for this lens is enabled by the tools of the mathematical framework of Picard-Lefschetz theory, which was re-introduced to the study of oscillatory integrals in physics by Witten (2010), and has subsequently been applied to the study of lensing (Feldbrugge et al. 2019; Jow et al. 2021; Shi & Xu 2021). Witten (2010) and Feldbrugge et al. (2019) give a detailed description of the theoretical and numerical application of Picard-Lefschetz theory to oscillatory integrals, but we will give a brief summary here which follows the description of the theory in Jow et al. (2021).

The goal is to compute integrals of the form

$$I = \int_{\mathbb{R}} dx e^{iS(x;\xi)}, \quad (\text{A1})$$

where ξ is a set of parameters that fix the phase function $S(x;\xi)$. Picard-Lefschetz theory is an application of Cauchy's theorem for the deformation of integration domains and guarantees the existence of a surface in the complex plane, \mathbb{C} , that is a continuous transformation of the original integration domain, \mathbb{R} , such that the integrand is localized and non-oscillatory.

To see how this works, we define the function $h(z) = \text{Re}\{iS(z)\}$. We assume that $S(z)$ is analytic, and we have replaced the integration variable x with the variable z to denote the analytic continuation of the integrand to the complex plane. It follows from the Cauchy-Riemann equations that the critical points of the function $h(z)$ are also the critical points of $S(z)$, and that the non-degenerate critical points are saddle points of the function h . Thus, every critical point z_i of $h(z)$ has associated with it a contour of steepest descent, \mathcal{J}_i , with a dimension of one, and a contour of steepest ascent, \mathcal{U}_i , of equivalent dimension.

The contours of steepest descent are determined by the flow equations

$$\frac{dz}{dt} = \mp \frac{d(i\bar{S})}{d\bar{z}}, \quad \frac{d\bar{z}}{dt} = \pm \frac{d(iS)}{dz}, \quad (\text{A2})$$

When the sign in front of the right-hand side of the first of Eq. (A2) is negative (and the sign of the second is positive), the equations

determine the trajectories of steepest descent. When the signs are reversed, the equation determines the trajectories of steepest ascent. The surface \mathcal{J}_i associated with z_i is a manifold determined by the set of initial points for which solutions to the steepest ascent equation terminate at z_i as $t \rightarrow \infty$. Hence, the surface \mathcal{J}_i is a contour of descent, since the direction pointing away from the critical point z_i along the surface \mathcal{J}_i is a direction of decreasing h .

One can show that along each of the contours of steepest descent, \mathcal{J}_i , the quantity $\text{Im}\{iS(z)\}$ is constant:

$$\frac{d\text{Im}[iS]}{dt} = \frac{1}{2i} \frac{d(iS + i\bar{S})}{dt} = \frac{1}{2i} \left(\frac{\partial(iS)}{\partial z} \frac{dz}{dt} + \frac{\partial(i\bar{S})}{\partial \bar{z}} \frac{d\bar{z}}{dt} \right) = 0. \quad (\text{A3})$$

Moreover, the total integrand exponentially approaches 0 away from the critical point. This means that the integrand is localized and non-oscillatory along these surfaces, which we call the ‘‘Lefschetz thimbles’’. Picard-Lefschetz theory guarantees that the integral along the original domain, \mathbb{R} , is equal to a sum of integrals along the Lefschetz thimbles. Explicitly,

$$I = \sum_i n_i \int_{\mathcal{J}_i} dz e^{iS(z;\xi)}, \quad (\text{A4})$$

where $n_i = \langle \mathbb{R}, \mathcal{U}_i \rangle$ is the intersection number, which counts the number of times the steepest ascent contour, \mathcal{U}_i , intersects the original integration domain, \mathbb{R} , with sign given by the relative orientations of the two curves. Thus, a thimble, \mathcal{J}_i , contributes to the integral if and only if the contour of steepest ascent, \mathcal{U}_i , for the corresponding critical point, z_i , intersects the original integration domain. In order to compute the integral for a given set of parameters, ξ , one must find the complex critical points of z_i , as well as the surfaces of steepest ascent and descent associated with each critical point, which can be achieved by solving the flow equations. Note that here we have given a brief description of Picard-Lefschetz theory for one-dimensional oscillatory integrals, but the theory may be extended to arbitrary dimension (see Witten 2010; Feldbrugge et al. 2019).

The topology of the Lefschetz thimbles in the complex domain varies smoothly with the parameters ξ except at caustics and Stokes lines. Caustics are points in parameter space where a set of real critical points become degenerate. Lensing near caustics has been widely studied in both the geometric and diffractive regimes (Nye 1999). Stokes lines are points at which the number of relevant complex critical points changes, and occur when the Lefschetz thimbles of multiple critical points overlap (see Witten (2010) and Jow et al. (2021) for a more detailed description of Stokes lines). Together, the caustics and Stokes lines form separate regions in parameter space where the Lefschetz thimble topology is distinct. Fig. A1 shows the different thimble topologies for the rational lens. The black and purple lines are the caustics and Stokes lines, respectively, which separate the parameter space into five distinct regions. The encircled diagrams for each region show the relevant thimbles in the complex domain. The red dots correspond to the relevant critical points, and the black and grey curves correspond to the surfaces of steepest descent and ascent associated with each critical point. The blue dots correspond to the poles of the analytically continued phase function. As defined in Eq. (1), the integral would be performed over the real axis and is conditionally convergent. However, Picard-Lefschetz theory guarantees that the integral over the relevant Lefschetz thimbles (the black curves in the encircled diagrams) is not only equal to the original integral over the real axis, but is absolutely convergent.

Note that the thimble topologies for the rational lens only depend on the parameters κ and y , as v is simply an overall factor

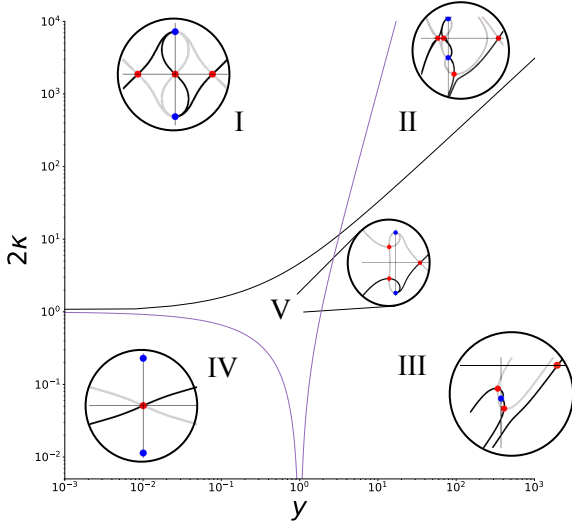


Figure A1. Lefschetz thimble topologies for the rational lens, $\psi = 1/(1 + x^2)$. The black and purple lines show the position of the caustics and Stokes lines in lens parameter space, which separate the regions (labeled I, II, III, IV, and V) with distinct thimble topology. The encircled diagrams show the topology of the relevant thimbles in the complex domain for each of these regions. The red dots correspond to the relevant critical points, and the black and grey curves correspond to the surfaces of steepest descent and ascent associated with each critical point. The blue dots correspond to the poles of the analytically continued phase function.

multiplying the exponent of the integrand in the Kirchhoff-Fresnel integral (Eq. (1)). Thus, ν does not affect the solution to the flow equations, and thereby does not affect the thimble topology. Positive values of γ are shown on the horizontal axis of Fig. A1 as the result of the Kirchhoff-Fresnel integral is symmetric about $\gamma = 0$ for the rational lens. The vertical axis is taken to be 2κ , as the cusp catastrophe occurs at $2\kappa = 1$.

One of the most powerful aspects of Picard-Lefschetz theory as applied to lensing is that it allows for the separation of the total integral into contributions associated with a discrete set of critical points, $\{z_i\}$, by performing the integral along the associated Lefschetz thimbles separately. Moreover, these critical points are precisely the images of geometric optics. Indeed, when $\nu \rightarrow \infty$, the value of the integral associated with each of the Lefschetz thimbles converges to the geometric optics value of the field for each image given by Eq. (4). Since Picard-Lefschetz theory gives an exact value of the integral for all values of ν , this essentially allows us to extend the image analysis of geometric optics to low frequencies.

As an example, consider when $\kappa = 5000$ and $\gamma = 1000$, which corresponds to Region II in Fig. A1. The total intensity fluctuations above unity for these parameters as a function of frequency is shown in the top middle panel of Fig. 4 (along with similar plots for the other regions). For these parameters, there are four relevant critical points, one complex and three real. We will label the complex critical point z_c and the real critical points x_0 , x_1 , and x_2 , with descending value. Fig. A2 shows the critical points and their corresponding Lefschetz thimbles in the complex domain. The background colour corresponds to the value of the function, $h(z)$. In general, Lefschetz thimbles terminate at poles of $h(z)$ or infinity. The thimble for x_2 goes from the pole at infinity to the pole at $+i$; the thimble for x_1 goes from the pole at $+i$ to $-i$; the thimble for z_c goes from $-i$

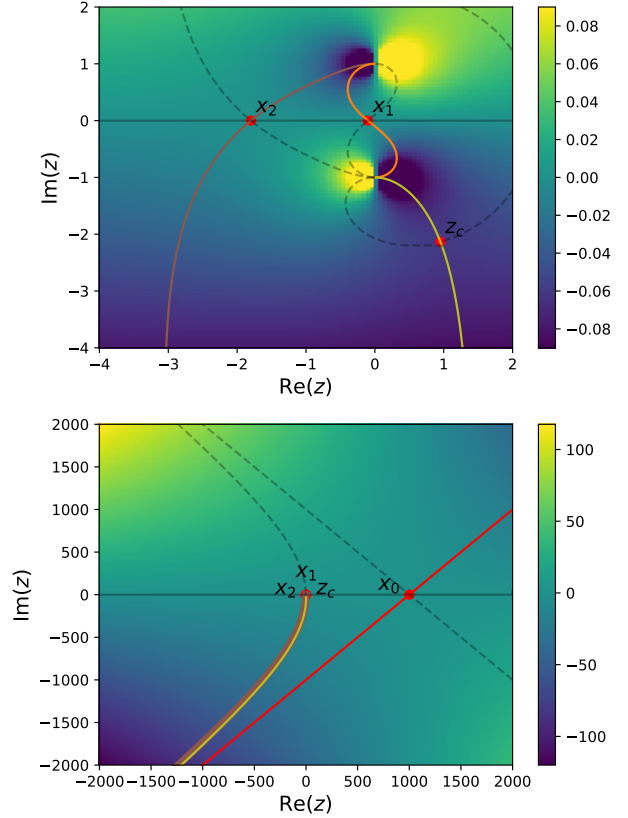


Figure A2. The Lefschetz thimbles in the complex plane for the rational lens, $\psi = 1/(1 + x^2)$, with $\kappa = 5000$ and $\gamma = 1000$. For these parameters there are three relevant real images, which have been labeled x_0 , x_1 , x_2 , and a single relevant complex image, z_c . The bottom panel shows a zoomed out view of the complex plane. The background colour is determined by the value of the function $h(z)$, evaluated for $\nu = 10^{-5}$. The Lefschetz thimbles are the surfaces of steepest descent in the function h from the critical points. The steepest ascent contours are shown as grey dashed lines, and the original integration contour, the real line, is shown as a solid grey line.

to infinity; and the thimble for x_0 goes from infinity in the lower half-plane to infinity in the upper-half plane.

By examining the integrand along each of these thimbles, we can see exactly how geometric optics fails at low frequencies. Fig. A3 shows the magnitude of the integrand evaluated along the thimbles for different values of ν . For large ν , the integrand generically takes the form of a single peak at the critical point, which decays exponentially away from the peak. As ν increases, the width of this peak decreases, and the integrand effectively becomes a delta function at the critical point. Thus, in the limit of $\nu \rightarrow \infty$, the contribution of each thimble is entirely determined by a small neighbourhood of the critical point, and geometric optics is recovered. However, as ν decreases, the effective region that contributes to the integral increases. This has two main effects. Firstly, since some of the thimbles terminate at poles, rather than infinity, at low frequencies the width of the integrand has become large enough that it effectively becomes cut off by the presence of the pole before it can decay to zero (see the integrands for z_c , x_1 , and x_2 for low frequencies in Fig. A3). Secondly, as the effective region that contributes to the integral increases, the curvature of the thimble becomes important. In the geometric limit, when the integrand is isolated to

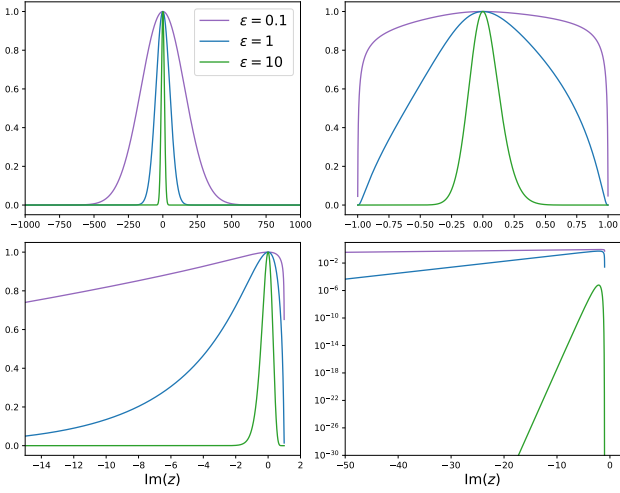


Figure A3. The absolute value of the integrand of the Kirchhoff-Fresnel integral, $\exp\{i\nu[\frac{(x-y)^2}{2} + \frac{\kappa}{1+x^2}]\}$, evaluated along the Lefschetz thimbles shown in Fig. A2 for $\kappa = 5000$ and $y = 1000$. From left to right, and top to bottom, the integrand is shown for the thimbles associated with x_0 , x_1 , x_2 , and z_c . The thimbles are parametrized by the imaginary component of the complex variable, $\text{Im}(z)$. The integrand is shown for multiple values of ν , such that $\epsilon \equiv \kappa\nu = 0.1, 1$, and 1 .

a small region about the critical point, only the local curvature of the thimble matters. In particular, the measure of the integral, dz , becomes $dz \propto \exp\{i[\frac{\pi}{4} - \frac{\arg(\Delta_j)}{2}]\}$ at the critical point. However, as the ν decreases, the curvature of the integration contour away from the critical point becomes relevant. While the location of the poles is independent of the lens parameters, the effective width of the integrand along the thimbles is determined by both ν and κ . In particular, it is when $\epsilon = \kappa\nu \gg 1$ that the integrand becomes localized to a small region on the thimble about the critical point with constant curvature. Thus, it is in this way that the parameter ϵ sets when geometric optics holds. Note that since the thimble for x_0 goes from minus infinity to positive infinity in a straight line (i.e. with constant curvature), neither of these effects is relevant, and, indeed, the contribution to the total integral computed along its Lefschetz thimble is always equal to the geometric optics prediction for all ν .

As an aside, the fact that near the critical point, the measure along the Lefschetz thimble becomes $dz \propto \exp\{i[\frac{\pi}{4} - \frac{\arg(\Delta_j)}{2}]\}$ is the origin of the extra phase factors in Eqs. 3 and 4. When the critical points are real, $\arg(\Delta_j) = 0$ or π . This binary choice of angle for real images is usually expressed as the statement that each real image has a Morse index, n_j associated with it, which is an integer of either 0 or 1. However, when the formalism is extended into the complex plane, we see that for complex images, the angle associated with the Lefschetz thimble is arbitrary, and so images, in general, do not have an associated integer Morse index.

Now, examining how the integrand behaves along the Lefschetz thimbles allows us to understand how geometric optics systematically fails as ν decreases. We can also look at how the integral evaluated along the thimbles separately behaves as a function of frequency. Fig. A4 shows the flux associated with each image as a function of frequency. That is, we compute the integral along each thimble separately and plot the absolute value squared of the result. In the high- ν limit, these values converge to the intensities $|F_j|^2$ for each of the images predicted by geometric optics. The grey dashed

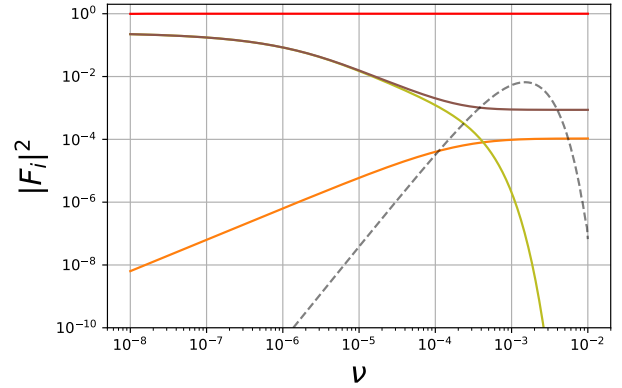


Figure A4. The magnitude squared of the contribution to the total Kirchhoff-Fresnel integral associated with the Lefschetz thimbles of x_0 (red), x_1 (orange), x_2 (blue), and z_c (green), for the rational lens with $\kappa = 5000$ and $y = 1000$. The thimbles and images are shown in Fig. A2. The grey dashed line shows the perturbative intensity fluctuations, $|F^{\text{pert}} - 1|^2$.

line in Fig. A4 shows the value of the intensity fluctuations in the perturbative expansion, $|F^{\text{pert}} - 1|^2$. We know from Fig. 4 that the total intensity computed using Picard-Lefschetz theory begins to agree with the perturbative below $\nu \sim 10^{-3}$; however, in Fig. A4 we find that the intensities of the individual images are, asymptotically, orders of magnitude larger than the perturbative intensity fluctuations. While this may seem strange at first glance, this is not contradictory. As $\nu \rightarrow 0$, we can see that the intensities of the images at z_c and x_2 become equal to each other. Their phases, however, become almost exactly opposite. This is easy to see from the bottom panel of Fig. A2. At large $|z|$, the thimbles associated with z_c and x_2 become anti-parallel. When $\nu \rightarrow 0$, the relevant region of integration along these thimbles gets larger, and so the values of the integral for these two images become roughly equal in magnitude but opposite in sign. Thus, while individually their intensities may be large, the magnitude of their sum is small. It turns out that this sum is close to opposite in phase with the image at x_1 , leading to a further cancellation. As a result, the intensity of the sum of the three images x_1 , x_2 , and z_c becomes very small, and, indeed, agrees with the perturbative intensity fluctuations (the intensity for the image x_0 is unity, independent of ν).

This gives us insight into how geometric optics becomes diffractive optics as ν decreases. In this case, a subset of the images become mutually coherent with each other, in such a way that they almost exactly cancel each other out. What is left is an unperturbed image (x_0 in this case) with a small modulation on top. We can perform the same exercise for the different regions shown in Fig. A1, and a similar picture emerges: the multiple images in the geometric picture attain the same or opposite phases in the limit as $\nu \rightarrow 0$, and their sum yields the perturbative expansion.

This paper has been typeset from a \LaTeX file prepared by the author.